THE PROTEIN SOCIETY

Concomitant disorder and high-affinity zinc binding in the human zinc- and iron-regulated transport protein 4 intracellular loop

Elizabeth M. Bafaro,[1] Mark W. Maciejewski,[2] Jeffrey C. Hoch,[2]* and Robert E. Dempski[1]*

[1]Department of Chemistry and Biochemistry, Worcester Polytechnic Institute, Worcester, Massachusetts 01609
[2]Department of Molecular Biology and Biophysics, UConn Health, Farmington, Connecticut 06030

Received 3 December 2018; Accepted 13 February 2019
DOI: 10.1002/pro.3591
Published online 12 March 2019 proteinscience.org

Abstract: The human zinc- and iron-regulated transport protein 4 (hZIP4) protein is the major plasma membrane protein responsible for the uptake of zinc in the body, and as such it plays a key role in cellular zinc homeostasis. hZIP4 plasma membrane levels are regulated through post-translational modification of its large, disordered, histidine-rich cytosolic loop (ICL2) in response to intracellular zinc concentrations. Here, structural characteristics of the isolated disordered loop region, both in the absence and presence of zinc, were investigated using nuclear magnetic resonance (NMR) spectroscopy. NMR chemical shifts, coupling constants and temperature coefficients of the apo-protein, are consistent with a random coil with minor propensities for transient polyproline Type II helices and β-strand in regions implicated in post-translational modifications. The ICL2 protein remains disordered upon zinc binding, which induces exchange broadening. Paramagnetic relaxation enhancement experiments reveal that the histidine-rich region in the apoprotein makes transient tertiary contacts with predicted post-translational modification sites. The residue-specific data presented here strengthen the relationship between hZIP4 post-translational modifications, which impact its role in cellular zinc homeostasis, and zinc sensing by the intracellular loop.

Abbreviations: CPMG, Carr–Purcell–Meiboom–Gill; csd, chemical shift displacements; DTT, dithiothreitol; EDTA, ethylenediaminetetraacetic acid; HSQC, heteronuclear single-quantum coherence; hZIP4, human zinc- and iron-regulated transport protein 4; ICL, intracellular loop; IDP, intrinsically disordered protein; IDR, intrinsically disordered protein region; INEPT, insensitive nuclei enhanced by polarization transfer; MTSL, 1-oxyl-2,2,5,5-tetramethylpyrroline-3-methyl)methane-thio-sulfonate; NMR, nuclear magnetic resonance; NOE, nuclear Overhauser enhancement; PMSF, phenylmethylsulfonyl fluoride; PPII, polyproline type II; PRE, paramagnetic relaxation enhancement; PTM, post-translational modification; RNMRTK, Rowland NMR Toolkit; SH3, Src homology 3; SSP, Secondary structure propensity; TCEP, Tris(2-chloroethyl) phosphate; TEV, tobacco etch virus; TM, transmembrane; ZIP, zinc- and iron-regulated transport protein.

Additional Supporting Information may be found in the online version of this article.

Grant sponsor: National Institutes of Health P41GM111135 R01 GM105964.

**Correspondence to:* Jeffrey C. Hoch, Department of Molecular Biology and Biophysics, UConn Health, Farmington, CT 06030. E-mail: hoch@uchc.edu or Robert E. Dempski, Department of Chemistry and Biochemistry, Worcester Polytechnic Institute, 100 Institute Road, Worcester, MA 01609. E-mail: rdempski@wpi.edu

Broader Impact Statement: Intrinsically disordered proteins often undergo coupled binding–folding in order to perform their biological functions. We find that the intracellular loop region of the zinc transporter human zinc- and iron-regulated transport protein 4 (hZIP4) remains disordered upon zinc binding, despite having a high affinity for zinc. As the intracellular loop regulates post-translational modification of hZIP4 in a zinc-dependent manner, the absence of a pronounced conformational change suggests an alternative mechanism in which changes in surface charge distribution upon zinc binding influence post-translational modification.

Furthermore, the zinc sensing mechanism employed by the ICL2 protein demonstrates that high-affinity interactions can occur in the presence of conformational disorder.

Keywords: zinc; intrinsically disordered protein; nuclear magnetic resonance; protein structure; transporter; hZIP4; intracellular loop; zinc sensing

Introduction

As the second most abundant transition metal in the body, zinc functions as a structural component in proteins, as a catalytic center in enzymes, and as a signaling molecule that regulates cellular signal transduction processes.[1–4] In keeping with its important cellular roles, pathophysiological consequences, including cardiovascular disease, depression, Alzheimer's disease, diabetes mellitus, and cancer, are associated with abnormal zinc levels.[5] The SLC39 or zinc- and iron-regulated transport protein (ZIP), family of proteins, act to increase cytosolic zinc concentrations by transporting zinc into the cytosol from the extracellular space or from intracellular compartments. Human (h) ZIP4 is expressed on the apical surface of enterocytes, where it functions as the primary transporter for the uptake of dietary zinc. Mutations in hZIP4 are responsible for the childhood zinc deficiency disease *acrodermatitis enteropathica*, whose symptoms include skin lesions, alopecia, diarrhea, neurological disorders, growth retardation, and death, if left untreated.[6–8] Changes in hZIP4 expression levels have also been observed in several cancers, including liver, brain, and pancreatic cancer.[9–12]

Recent structural studies have shed light on the metal translocation pathway in hZIP4. hZIP4 has eight transmembrane (TM) segments and a large extracytosolic N-terminal domain. A computational model of the hZIP4 TM domain predicted that metals are translocated through a helical bundle formed by TMs 2, 4, 5, and 7,[13] which was confirmed in the crystal structure of a prokaryotic ZIP protein.[14] Also, functionally significant is the large extracellular N-terminal domain of hZIP4, as it has been shown to be required for optimal zinc transport,[15] and many *acrodermatitis enteropathica* mutations map to this region.[8,16,17] In the absence of zinc, the crystal structure of an ectodomain of a ZIP4 homologue adopts a dimeric fold consisting of a helix-rich region and a helix-turn-helix region containing a histidine-rich sequence, which has been hypothesized to function as an extracellular zinc sensor.[15]

In contrast to the recent structural data for the TM and N-terminal domains of ZIP proteins, few structural details are known about the largest intracellular loop between TM3 and TM4 (ICL2) [Fig. 1(a)]. ICL2 is not highly conserved among the hZIP family (Supporting Information Fig. S1), suggesting that the loop has different functions in hZIP homologues. hZIP4 ICL2 is hypothesized to act as an intracellular zinc sensor that regulates plasma membrane levels of the hZIP4 protein. As cytosolic zinc concentrations increase presumably via hZIP4 transporter activity, hZIP4 is ubiquitinated at a lysine residue within ICL2 and is subsequently degraded.[18] This post-translational regulation requires a histidine-rich sequence within ICL2 [Fig. 1(b)].[18] The histidine-rich region of the isolated ICL2 was shown to bind two zinc ions sequentially, with the first zinc binding with nanomolar affinity to a $CysHis_3$ site and the second zinc binding to a His_4 site.[19] Sequence analysis predictions and circular dichroism spectroscopy indicate that ICL2 is an intrinsically disordered protein region (IDR).[19]

Intrinsically disordered proteins (IDPs) and IDRs, which lack stable secondary and tertiary structure, are abundant in nature, constituting approximately 20% of eukaryotic proteomes.[20] Over 40% of human plasma membrane proteins are predicted to contain regions of disorder with these regions more likely to occur on the cytoplasmic side.[21] Disordered regions are not evolutionarily conserved in protein families,[22] as is the case for hZIP ICL2 regions (Supporting Information Fig. S1). Disordered protein regions perform a number of important biological functions including ligand binding, protein–nucleic acid interactions, and protein–protein interactions. Different interaction mechanisms have been observed for IDPs/IDRs, ranging from complete folding upon binding to the formation of dynamic or "fuzzy" complexes, in which the interacting proteins remain conformationally disordered.[23–25] IDP/IDR interactions have generally been viewed as occurring with high specificity but low affinity.[26–28] This view has been used to explain the importance of structural flexibility in cellular signaling processes, where IDPs/IDRs have been shown to interact with multiple targets and to undergo multiple post-translational modifications (PTMs).[25] The high-specificity, low-affinity view of IDP/IDR interactions has been challenged by recent observations of disordered protein–protein interactions that form high-affinity "fuzzy" complexes via nonspecific interactions.[29,30]

The unique biophysical properties of IDPs/IDRs, which exist as dynamic ensembles of heterogeneous conformations, have presented challenges to their structural characterization. Nuclear magnetic resonance (NMR) spectroscopy is an established and powerful technique that provides atomic level information on the conformational ensembles sampled by IDPs/IDRs in physiological solution conditions.[31–33] Here, we have investigated the structural ensemble of the apo form and the zinc-bound forms of the disordered hZIP4 ICL2 region using NMR spectroscopy. Using NMR chemical shift analyses, coupling constants, and temperature coefficients, the

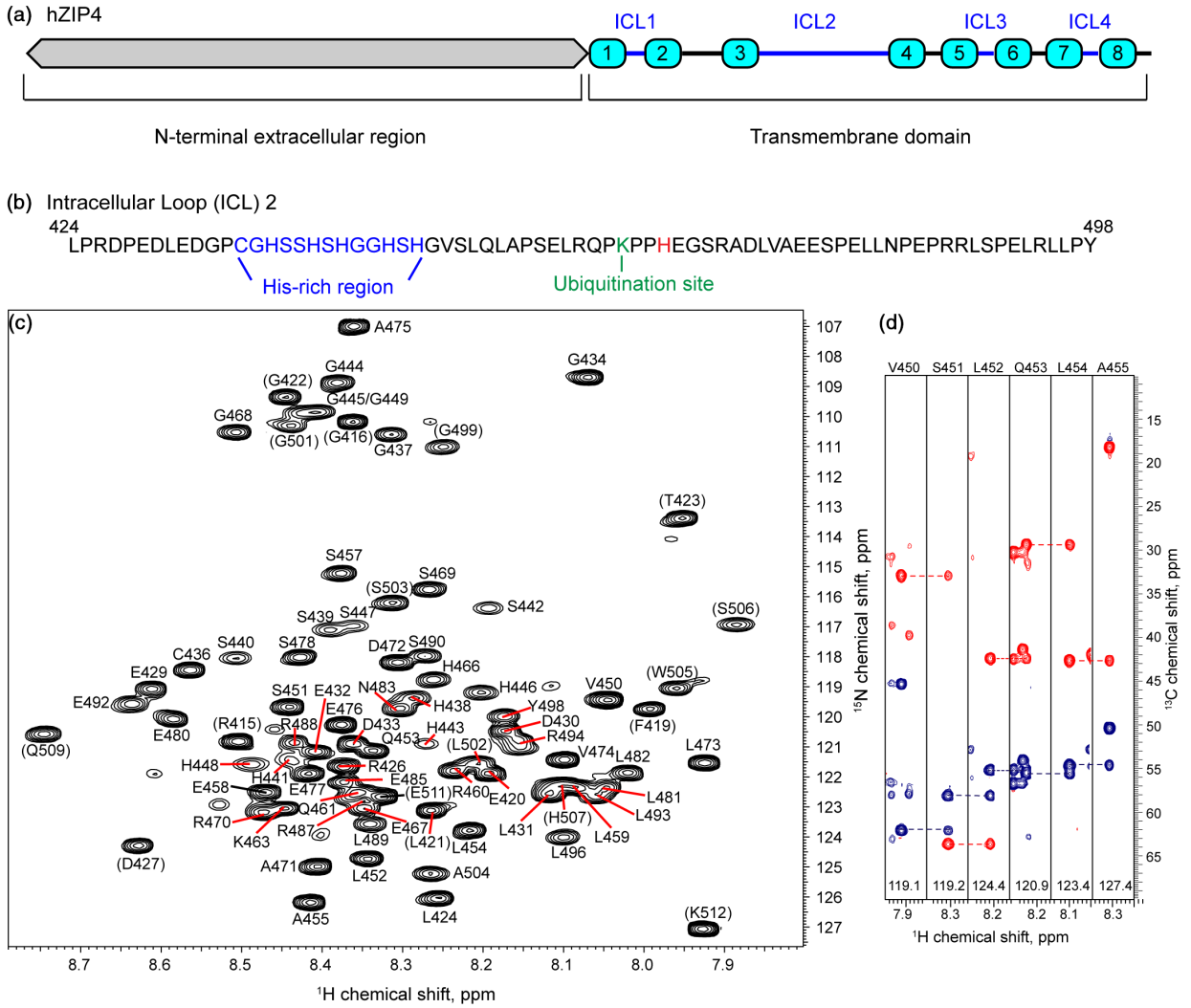

Figure 1. hZIP4 ICL2 location NMR data and assignments. (a) Schematic representation of the domain structure of hZIP4. The large extracellular, N-terminal domain is indicated in gray, and the TM segments are indicated in cyan. Intracellular loops, depicted with blue lines and labeled, are drawn to scale. (b) Amino acid sequence of ICL2. The histidine-rich region is highlighted in blue, the single histidine (H466) outside the histidine-rich region is indicated in red, and the ubiquitination site (K463) is indicated in green. (c) ^{1}H-^{15}N HSQC spectrum (800 MHz) of the isolated hZIP4 ICL2 (300 μ*M*) in 20 m*M* Hepes (pH 7), 20% glycerol, and 5 m*M* TCEP at 10°C. The peak for A475 is aliased in the ^{15}N dimension; the ^{15}N resonance for A475 is 127.45 ppm. Amino acid numbering corresponds to the position in the hZIP4 full-length protein sequence. Residues in parentheses are cloning scars and the purification tag. (d) Two-dimensional planes from the HNCACB experiment measured at 25°C indicate sequential assignment along the hZIP4 ICL2 backbone.

average ICL2 ensemble exhibits random coil behavior with minor tendencies for polyproline Type II (PPII) helices and β-strand at several regions encompassing sites predicted to be post-translationally modified. Further, these sites make contacts with the histidine-rich, zinc-binding region of ICL2 as revealed by paramagnetic relaxation enhancement (PRE) experiments. Metal binding does not detectably alter the disordered landscape of the ICL2 protein ensemble. Zinc binding induces exchange broadening, indicating that the metal-bound ICL2 protein undergoes dynamic interchange among two or more metal-bound states. Together, our data provide structural evidence supporting the hypothesis that ICL2 acts as an intracellular zinc sensor to regulate plasma membrane levels of hZIP4 and maintain cellular zinc homeostasis.

Results

NMR resonance assignments and local secondary structure conformational propensity

The largest intracellular loop of hZIP4, ICL2, was shown previously by sequence analysis and circular dichroism spectroscopy to be an IDR.[19] NMR has become a powerful technique to study the conformational heterogeneity of disordered proteins.[31] To increase the yield of the isolated loop region for NMR studies, an inclusion body-targeted expression system based on fusion to a signal sequenceless *Escherichia coli* outer membrane protein, PagP, was employed.[34,35] The resulting purified ICL2 protein (Supporting Information Fig. S2), in NMR buffer containing 5 m*M* Tris (2-chloroethyl) phosphate (TCEP), showed comparable

binding affinity for zinc (6 ± 2 n*M*) as measured previously in buffer containing 100 μ*M* TCEP and 150 m*M* sodium chloride (6 ± 1 n*M*).[19] In addition, ^{1}H-^{15}N heteronuclear single-quantum coherence (HSQC) spectra of isolated ICL2 protein prepared as described previously[19] and prepared using the inclusion body-targeted expression system were identical (Supporting Information Fig. S2).

The ^{1}H-^{15}N HSQC spectrum of hZIP4 ICL2 measured at 10°C [Fig. 1(c)] displays a narrow chemical shift dispersion in the ^{1}H dimension ranging from 7.8 to 8.8 ppm. Reduced chemical shift dispersion in the ^{1}H dimension is characteristic of IDRs compared to spectra for folded proteins.[36] Backbone assignments at 10°C were completed by using HNCO, HN(CA)CO, HNCACB, and CBCA(CO)NH experiments conducted at 25°C [Fig. 1(d)] and by sequential assignment of short-range nuclear Overhauser enhancement (NOE) resonances using a ^{15}N-edited NOESY-HSQC spectrum. Chemical shift changes in the HSCQ spectrum were followed as the temperature decreased from 25°C to 10°C. Additional cross-peaks, corresponding to residues within the histidine-rich region that were absent at 25°C, were observed in the HSQC spectrum as the temperature decreased and these were assigned using mutant proteins (H441A, S442A, H443A, and H446A). Finally, 72 of the 76 nonproline main chain amides were assigned unambiguously in the NMR spectrum [Fig. 1(c)]. G445 and G449 could not be assigned unambiguously due to spectral overlap. Also, L495 could not be assigned, likely also due to spectral overlap, and the N-terminal glycine was not visible in the spectrum.

To explore the possibility of residual structure in ICL2, secondary chemical shifts, $^{3}J_{\mathrm{HN\text{-}H\alpha}}$ coupling constants, and temperature coefficients were examined. Chemical shifts, which are sensitive indicators of dihedral angles in the peptide backbone, are routinely used to identify secondary structure elements in proteins.[37,38] For IDRs, chemical shifts are averages of all transient conformations. Transient secondary structure elements in IDRs have been identified using secondary chemical shifts, or the difference between the measured chemical shift and reference random coil values.[39] Secondary chemical shifts for ICL2 were calculated using two random coil references.[39,40] Values for secondary chemical shifts were small (Supporting Information Fig. S3), suggesting that the ICL2 protein region exists predominantly as a random coil. Transient secondary structure populations for the disordered hZIP4 ICL2 were assessed using both the secondary structure propensity (SSP) score[41] and the δ2D method.[42] Both methods (Fig. 2) indicated that the ICL2 protein region is largely random coil with slight tendencies for regions of β-strand between residues 460–469 and 484–490. The δ2D method also suggested a minor propensity of PPII secondary structure across the polypeptide [Fig. 2(b)]. These residues also show decreased cross-peak heights (Supporting

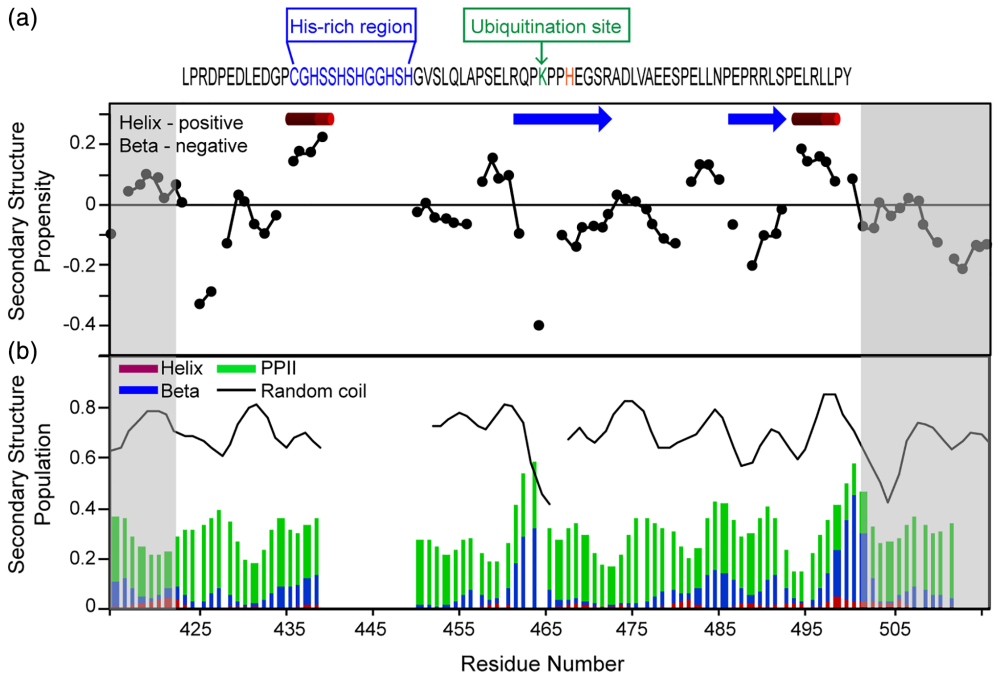

Figure 2. Secondary structural elements for the isolated ICL2 region. (a) SSP values calculated using Cα and Cβ resonances measured at 25°C. Positive values represent fractional α helix populations, and negative values represent fractional β-strand populations. (b) Secondary structure populations predicted from chemical shifts measured at 25°C using the δ2D method. Secondary structures are colored red for α-helix, blue for β-strand, and green for PPII. The black line indicates the random coil population. Shaded regions indicate the protein tag sequences at the N- and C-termini. Resonances for 438–449 are missing in the spectra at 25°C and were not included in the analyses.

Information Fig. S4) further supporting that these regions are undergoing exchange between conformers with different secondary structure. Values of $^{3}J_{HN\text{-}H\alpha}$ coupling constants (Supporting Information Fig. S5) and temperature coefficients (Supporting Information Fig. S6), both of which have been used to identify regions of structure,[43] support the conclusion that the hZIP4 ICL2 apoprotein exists primarily in a random coil state in solution.

Zinc binding

Previously, the hZIP4 ICL2 was shown to coordinate two zinc ions with the first zinc binding at a $CysHis_3$ site and the second zinc binding at a His_4 site.[19] The single cysteine residue (C436) was responsible for the nanomolar binding affinity of zinc to ICL2.[19] Although previous data suggested that the residues involved in the two coordination sites are C436, H438, H441, H443, H446, and H448,[18,19] the exact binding sites could not be unequivocally identified. To ascertain the residues involved in zinc coordination, ^{1}H-^{15}N HSQC spectra were obtained in the presence of one and two molar equivalents of zinc [Fig. 3(a)]. The ^{1}H chemical shift peak dispersion of zinc-bound ICL2 remained narrow, indicating that the protein remained disordered upon zinc binding. The most prominent change in the spectra upon zinc addition was the disappearance of cross-peaks. Analysis of the peak heights [Fig. 3(b)] revealed a metal-dependent signal broadening with cross-peaks for residues in the histidine-rich region (residues 431–448), exhibiting ~50% reduction in signal with one zinc bound and complete signal broadening in the presence of two molar equivalents of zinc. Uniform signal broadening was observed in the histidine-rich region during a zinc titration with ICL2 (Supporting Information Fig. S7), precluding identification of the individual amino acids that coordinate each zinc ion. Significant signal broadening was also observed for residues D427 and E429, as well as V450, S451, and L452; however, no other residues exhibited metal-dependent signal broadening. Only small chemical shift deviations were observed for residues in and adjacent to the histidine-rich region, as well as for H466 and E467 [Fig. 3(c)]. Addition of ethylenediaminetetraacetic acid (EDTA) to the protein containing two molar equivalents of zinc reversed the effects of metal binding on both the cross-peak intensities and the chemical shift perturbations (Supporting Information Fig. S8). ^{15}N-edited NOESY-HSQC spectra of the apoprotein and protein with two equivalents of zinc showed identical NOE patterns (Supporting Information Fig. S9), which may indicate either the absence of intramolecular NOEs or, more likely, the averaged structural ensembles of the apoprotein and zinc-bound proteins are indistinguishable.

To examine further the role of histidines in zinc binding to ICL2, side chain ^{1}H-^{15}N HSQC spectra were acquired for the apoprotein and the protein with one and two molar equivalents of zinc added (Fig. 4). Chemical shifts for the δ1 and ε2 nitrogen are indicators of the protonation, tautomeric, and hydrogen

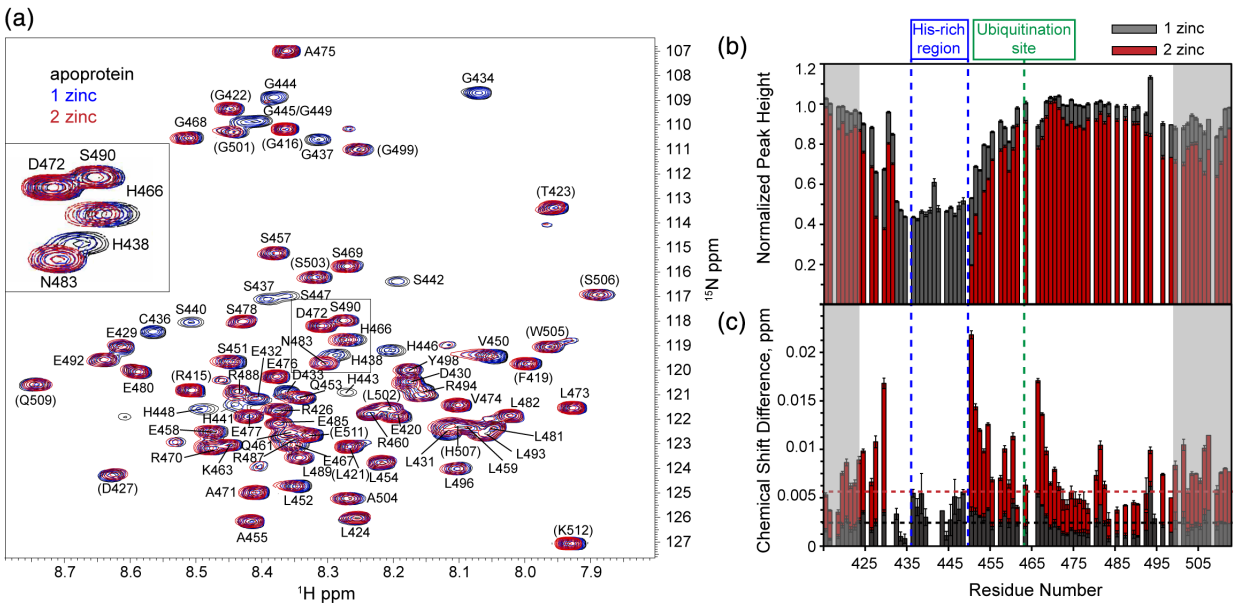

Figure 3. Zinc coordination by hZIP4 ICL2 affects the NMR observables for the histidine-rich region. (a) ^{1}H-^{15}N HSQC spectra of 300 μ*M* ICL2 at 10°C in the absence (black) and presence of one (blue) and two (red) equivalents of zinc. The peak for A475 is aliased in the ^{15}N dimension; the ^{15}N resonance for A475 is 127.45 ppm. The inset shows an expanded view of the boxed region. (b) Peak heights for ICL2 with one and two equivalents of zinc were normalized to the peak heights for the apoprotein. (c) Average $^{1}H^{N}$ and ^{15}N chemical shift deviations for ICL2 with one equivalent of zinc (gray) and two equivalents of zinc (red). The dashed lines represent the average chemical shift deviation across all measured residues for one zinc (black line) and two zinc (red line). In (b) and (c), shaded regions indicate the protein tag sequences at the N- and C-termini. Missing data points represent prolines and unassigned residues.

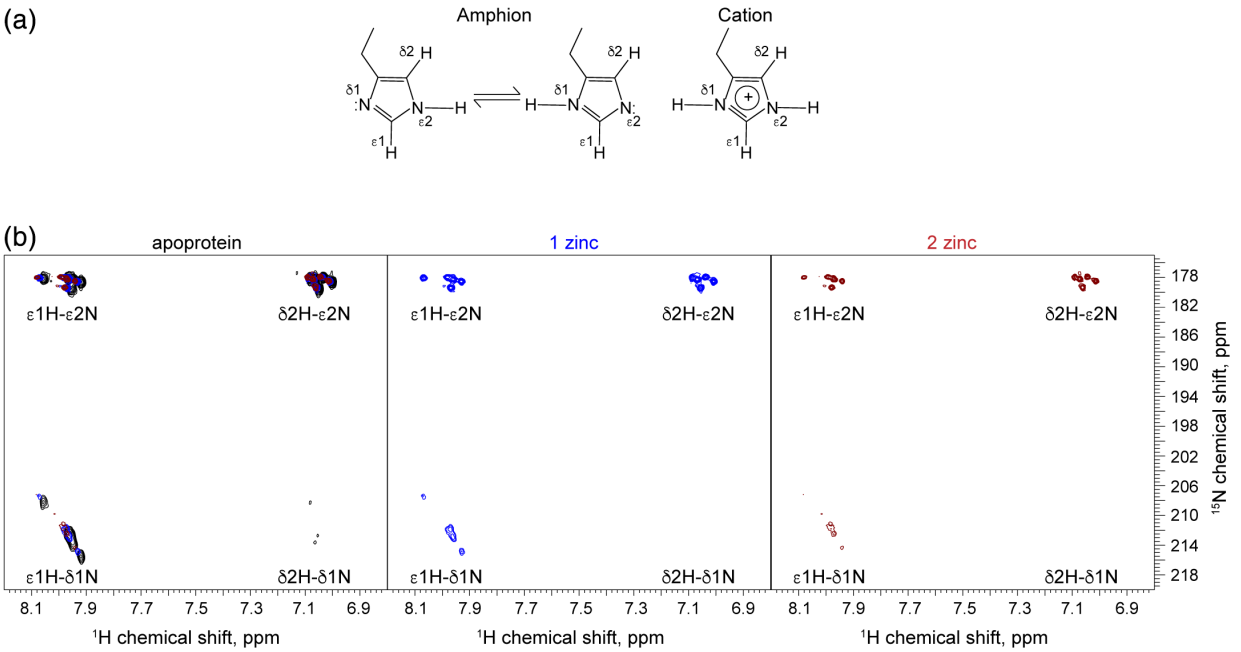

Figure 4. Zinc binding perturbs histidine side chains. (a) Tautomeric and protonation states of histidine side chains. (b) ^{1}H-^{15}N HSQC side chain spectra were acquired at 10°C and 800 MHz using coherence transfer from ε1H and δ2H to ε2N and δ2N through ^{2}J coupling constants as described in Materials and Methods section. Spectra were acquired for apoprotein (left, black) and one zinc-bound (center, blue) and two zinc-bound (right, red) forms at 300 μ*M*.

bonding states of the imidazole side chain.[44] For apo-ICL2 at pH 7, the δ1N chemical shifts range from 208 to 216 ppm, and the ε2N chemical shifts are ~178 ppm, which suggests an equilibrium between the amphionic (nonprotonated) states and the cationic state. Furthermore, the ε2N chemical shifts suggest that the histidine side chains are involved in hydrogen bonding.[45] Of the eight histidines present in the protein, only five correlations were clearly identified in the apoprotein spectrum (Fig. 4), which may be due to significant peak overlap. Upon addition of zinc, the peaks were significantly broadened (Fig. 4). The broadening was difficult to quantify as a result of the overlapping peaks. However, in general, the intensities of the ε2N peaks decreased 50%–60% upon binding one zinc ion and 25%–30%, relative to the apoprotein, upon binding the second zinc. The δ1N peaks were broadened more severely, with many peaks disappearing completely in the protein coordinated with two zinc ions. These data are consistent with the backbone amide cross-peak broadening observed across the histidine-rich region (Fig. 3).

Backbone dynamics and the effects of zinc binding

Relaxation measurements that explore the picosecond–nanosecond timescale motions of the polypeptide backbone are useful probes for investigating disordered proteins.[31] $^{15}N\{^{1}H\}$ heteronuclear NOE values and ^{15}N R_1 and R_2 relaxation rates were measured for the ICL2 apoprotein and in the presence of one and two molar equivalents of zinc (Fig. 5; Supporting Information Fig. S10). Heteronuclear NOE values for the apo- and zinc-bound proteins were largely identical, with values ranging between 0.4 and 0.6 at 800 MHz [Fig. 5(a)]. Heteronuclear NOE values above 0.6 at 800 MHz have been categorized qualitatively as characteristic of structured, rigid proteins, whereas values less than 0.2 are characteristic of unstructured, random coil.[46] The heteronuclear NOE values observed for ICL2 indicate an intermediate state between fully unstructured and structured protein.

Average R_1 relaxation rates for the apoprotein were 1.44 ± 0.09 and 1.41 ± 0.10 s^{-1} at 50 and 300 μ*M* protein concentrations, respectively, and residue-specific R_1 values showed comparable trends across the sequence for both protein concentrations (Supporting Information Fig. S10). These data are consistent with one or both of two possible mechanisms. Although the apoprotein population is predominantly monomeric, there is a small population of an oligomeric species. The oligomeric species is likely the cysteine-oxidized dimer identified by nonreducing sodium dodecyl sulfate polyacrylamide gel electrophoresis (Supporting Information Fig. S2). Alternatively, the small decrease in R_1 rates may be as a result of an increase in viscosity at the higher protein concentration. Overall, R_1 rates for protein with one and two molar equivalents of zinc were similar to the apoprotein, indicating that there is no metal-induced oligomerization [Fig. 5(b); Supporting Information Fig. S10].

Similar to R_1 rates, R_2 rates for the apo- and metal-bound proteins were comparable except in the histidine-rich region. Average R_2 rates (9 ± 2 s^{-1} for the apoprotein) are consistent with the disordered nature of

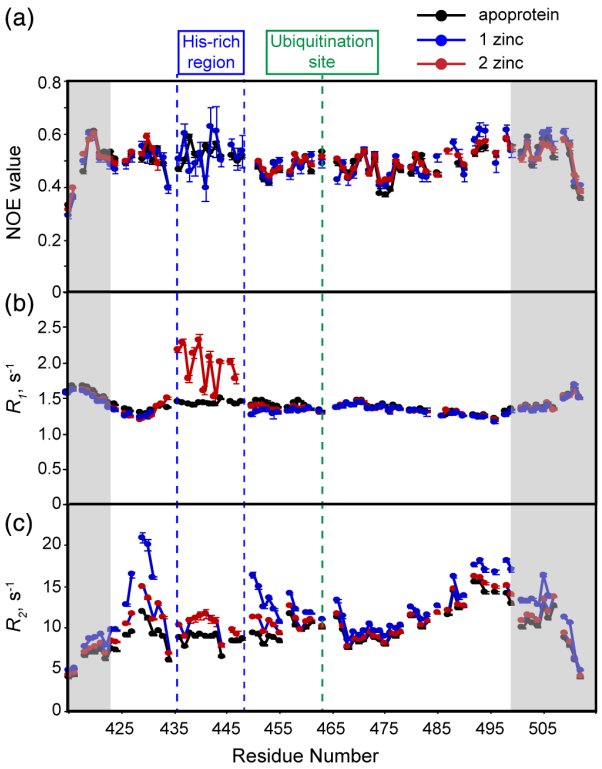

Figure 5. Dynamic characterization of the isolated ICL2 region in the absence (black) and presence of one (blue) and two molar equivalents of zinc (red). (a) ^{15}N-^{1}H heteronuclear NOEs, (b) ^{15}N longitudinal relaxation rates (R_1), and (c) ^{15}N transverse relaxation rates (R_2) for individual amide groups. All relaxation measurements were carried out with 300 μ*M* protein at 81 MHz and 10°C. Relaxation data for 50 μ*M* protein is given in Supporting Information Figure S10. Shaded regions indicate the protein tag sequences at the N- and C-termini. Missing data points represent prolines and unassigned residues.

the protein and reflect the temperature and glycerol content of the solvent, where glycerol has been shown to increase transverse relaxation rates two-fold.[47] Slightly reduced R_2 rates were observed as the protein concentration decreased (Supporting Information Fig. S10) as a result of a small population of cysteine oxidized dimer. Similar R_2 profiles were observed for the apo- and zinc-bound proteins at both low and high protein concentrations, indicating that the monomer–dimer equilibrium does not influence any exchange processes that may be occurring. Residue-specific R_2 relaxation rates for the apoprotein were higher for the C-terminal residues 492–498 [Fig. 5(c)], suggesting conformational exchange on the microsecond to millisecond timescale. Exchange on the millisecond time scale was probed using Carr–Purcell–Meiboom–Gill (CPMG)-based relaxation dispersion experiments. No significant dispersion was observed for any of the backbone amides (Supporting Information Fig. S11), indicating the absence of exchange on the millisecond time scale. Exchange occurring on faster time scales may contribute to the increased R_2 rates near the C-terminus. Compared to the apoprotein, zinc addition had the greatest effect on R_2 rates in the histidine-rich, zinc-binding region; however, the R_2 values in this region were too large to estimate due to the significant line broadening [Fig. 5(c)]. Elevated R_2 rates in the metal-binding region suggest conformational exchange on the micro to millisecond time scale between multiple metal bound states.

Global conformational preferences

Long-range structure in hZIP4 ICL2 was probed using PRE NMR experiments, which provide information on transient tertiary interactions in disordered proteins.[48] First, a paramagnetic nitroxide spin label, (1-oxyl-2,2,5,5-tetramethylpyrroline-3-methyl)methane-thio-sulfonate (MTSL), was introduced into the apoprotein at the single cysteine (C436) that is involved in zinc coordination. The location of the label enables identification of contacts between the zinc-binding region and distal parts of the protein. Backbone ^{15}N and ^{1}H^{N} resonances of the diamagnetic MTSL-labeled protein were identical to the unlabeled wild-type chemical shifts, with the exception of residues immediately adjacent to the spin-labeled C436, indicating that the spin label did not disturb the native conformational ensemble of the protein. The observed PRE effects were intramolecular as no significant interactions were observed in the control experiment containing ^{14}N-wild-type-ICL2-MTSL and ^{15}N-C436A-ICL2 (Fig. 6).

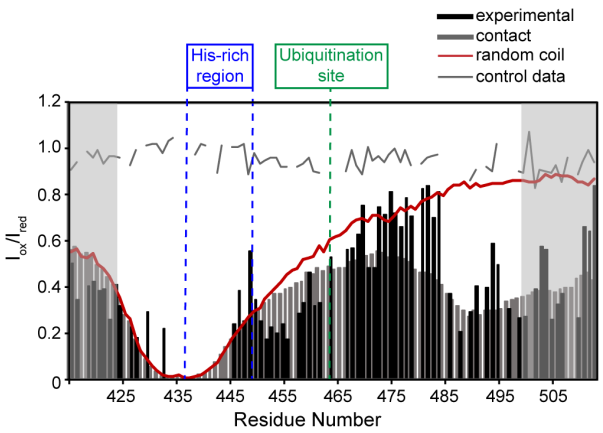

Figure 6. PRE measurements of ICL2 identify long-range interactions between the histidine-rich region and C-terminal residues in the apoprotein. PRE intensity ratios for 50 μ*M* MTSL-labeled ^{15}N-ICL2(C436) were calculated for backbone amide protons from ^{1}H-^{15}N HSQC spectra measured at 10°C in paramagnetic (oxidized) and diamagnetic (reduced) conditions. Theoretical PRE intensity ratios calculated for a simulated random coil ensemble with no contact restraints (red line) and for a random coil ensemble with contacts between residues 435–437 and 452–455 and between residues 435–437 and 489–498 (dark gray bars) were generated using *flexible-meccano.* The control experiment (gray line), performed with 50 μ*M* MTSL-labeled ^{14}N-ICL2(C436) and 50 μ*M* ^{15}N-ICL2(C436A), validated that the PRE effects resulted from intramolecular interactions. Shaded regions indicate the protein tag sequences at the N- and C-termini. Missing data points represent prolines and unassigned residues.

For 50 μ*M* ^{15}N-wild-type-ICL2-MTSL, ^{1}H-^{15}N cross-peak intensities were measured in the paramagnetic (I_{ox}) and diamagnetic (I_{red}) states, and intensity ratios indicate PRE effects within 25 Å of the probe. Experimental PRE ratios were compared with values calculated for a simulated statistical coil ensemble generated by *flexible-meccano* (Fig. 6). As expected, the largest PRE effects were observed for amino acids adjacent to the MTSL-labeled C436 (Fig. 6), with complete broadening of resonances for residues 433–443, indicating proximity within 12 Å of the probe. Outside these short-range effects, observed PRE ratios were smaller than predicted for the random coil model in several regions. Medium-range contacts were observed between the spin label at position 436 and residues 449–461, and long-range contacts were observed between the spin label at 436 and residues 470–471 and 485–498 (Fig. 6). Because the experimental PRE values did not match the random coil values, we computed a new ensemble using *flexible-meccano* with distance restraints of 15 Å between C436 and residues 452–455 and residues 489–498. The calculated PRE values for the constrained ensemble correlate more closely to the experimental data (Fig. 6). These data support a model in which the histidine-rich, zinc-binding region of ICL2 makes transient contacts with distal parts of the protein, in the absence of zinc.

Discussion

The largest intracellular loop of ZIP4, ICL2, regulates the plasma membrane levels of the transporter in response to intracellular zinc levels.[18] At low intracellular zinc concentrations, ZIP4 undergoes endocytosis from the plasma membrane, and as zinc concentrations increase, ZIP4 is ubiquitinated at the single lysine residue (K463) and proteolytically degraded.[18,49] Previously, we have shown that ICL2 is predicted to be an IDR that binds zinc via a histidine-rich region.[19] To gain further insight into the molecular basis for its role in zinc sensing by hZIP4, we have utilized NMR spectroscopy to characterize the structural properties of the isolated ICL2 region and in coordination with zinc.

NMR measurements, including chemical shifts, $^{3}J_{HN\text{-}H\alpha}$ coupling constants, and temperature coefficients, not only confirmed the disordered nature of the isolated ICL2 region but also indicated that, unlike other examples of IDPs and IDRs, the protein lacks any prominent, localized regions of secondary structure. On the basis of secondary chemical shift analysis, minor populations of PPII, as well as weakly populated β-strands, were predicted at two regions (460–465 and 482–492) that are known or predicted to be involved in post-translational modifications.[19] These two regions (460–465 and 485–492) also make transient, tertiary contacts with the histidine-rich, zinc-binding region of the isolated ICL2 protein as determined use PRE NMR experiments. The region 460–465 is known to undergo zinc-dependent ubiquitination at K463 and is a predicted binding site for Src homology 3 (SH3) domains.[18,19] SH3 domains, which have roles in membrane localization and protein phosphorylation, recognize and bind to PPII helices.[50] In addition, the C-terminal region (residues 482–492) is predicted to contain sites for protein phosphorylation.[19] Phosphorylation sites are preferentially found within PPII conformations in IDRs,[51] and it has been suggested that IDRs interact with protein partners involved in post-translational modification via a PPII to β-strand transition.[52,53] Phosphorylation of serine residues within the ICL2 of hZIP7 has been shown to stimulate zinc transport activity.[54] Although the conformational preferences of the isolated protein region may not reflect the states of the full-length hZIP4 transporter, an interaction between the histidine-rich region and the ubiquitination site (K463) was suggested previously as mutation of the histidine-rich region prevented hZIP4 ubiquitination.[18] Our PRE data demonstrate that, at least in the case of the isolated ICL2 region, the histidine-rich region makes transient contacts with the ubiquitination site and supports a model in which the ICL2 region acts as a zinc sensor that regulates plasma membrane levels of hZIP4.

Previously, we showed that the histidine-rich region coordinates two zinc ions sequentially, with the first zinc binding with nanomolar affinity to a $CysHis_3$ site and the second zinc binding with lower affinity to a His_4 site.[19] The near-complete backbone assignments for the isolated ICL2 prompted us to use NMR to pinpoint the zinc coordinating residues. However, the two zinc-binding sites could not be distinguished due to a zinc concentration-dependent loss of signal intensity for both the backbone amide protons in the histidine-rich region and the histidine side chain correlations. The zinc-induced line broadening was unexpected as the nanomolar affinity of the protein for the first zinc ion suggests slow exchange characteristics rather than the intermediate exchange processes observed. Intermediate exchange may occur either between two or more metal-binding sites or between different bound conformations. Intermediate exchange processes were proposed to explain the zinc-dependent signal broadening observed for the IDP amyloid β, which binds a single zinc with micromolar affinity.[55] Similarly, signal broadening was observed for zinc binding to peptide fragments of the extracellular domains of two ZIP family members, revealing a Cys_3 zinc-binding site in hZIP13[56] and a $CysHis_2Glu$-binding site in the *Arabodopsis* IRT1.[56,57] In contrast, zinc binding to the IDP α-synuclein produced chemical shift changes consistent with fast exchange, revealing two independent, noninteracting zinc-binding sites with weak (millimolar) affinity.[55] Unlike amyloid-β and α-synuclein, ICL2 exhibits a higher affinity for the binding of the first zinc ion, and the intermediate exchange characteristics observed upon zinc coordination by ICL2 are surprising and significant. We propose that interaction between the nanomolar zinc-binding site and the weaker affinity zinc-binding site in ICL2 results in zinc-induced line

broadening due to an overall intermediate exchange between multiple, transient zinc binding modes within the histidine-rich region of ICL2. This is supported by our previous X-ray absorption spectroscopy data indicating that the two zinc-binding sites in ICL2 are not independent.[19] An extension from our previous study, these data indicate that a single ICL2 zinc-bound state does not exist, but rather the one zinc-bound state is likely a conformational ensemble with the zinc coordinated by cysteine and multiple combinations of histidines. Flexible ligand binding sites were also observed for copper binding to the histidine–methionine-rich sequence on the lumenal loop of the copper transporter ATP7A.[58] As was speculated for ATP7A,[58] preference for a particular zinc coordination site in the intracellular loop of hZIP4 may be stabilized by interactions with metal chaperones or other protein partners involved in PTMs. Furthermore, PTMs, such as phosphorylation, may stabilize specific zinc-coordinating ligands within the histidine-rich region.

The ICL2 protein remains disordered in the metal-bound state(s). Although coupled binding and folding has been shown for some IDPs,[26,59–61] the concept of "fuzzy" complexes, in which the IDP/IDR remains conformationally flexible upon binding, has been demonstrated for many IDP interactions.[24,62,63] Although it has been generally believed that "fuzzy" complexes form because of weak interactions,[24,64] recent examples provide evidence that disordered protein–protein interactions can occur with high affinity even though the complex remains unstructured.[29,30] For example, the complex between the IDPs histone H1 and prothymosin-α is highly disordered and, yet the proteins interact with high (picomolar) affinity.[29] Additionally, a tight-binding (nanomolar) "fuzzy" complex was observed between the proline-rich motif of the viral nonstructural protein 1 and SH3 domain.[30] While these examples demonstrate that high affinity and disorder occur in protein–protein interactions, our data similarly show that the hZIP4 ICL2 region remains conformationally disordered in the presence of its high-affinity zinc ligand. Furthermore, no other tight-binding interactions between IDPs/IDRs and small molecules or ions have been reported previously.[28] To our knowledge, the ICL2-zinc ion interaction is the first example of a high-affinity, "fuzzy" complex between an IDP/IDR and a small ligand. It will be of interest to identify other IDPs/IDRs that form high-affinity, "fuzzy" complexes with small molecules or metal ion ligands to gain a better understanding of their prevalence and functional significance in biological systems.

Conclusion

Our results demonstrate that the hZIP4 ICL2 isolated protein is conformationally heterogeneous in the apo- and metal-bound states. No significant structural differences between the apo- and zinc-bound protein forms were discernable on the basis of the chemical shift data presented here. As the chemical shifts for both the apo- and zinc-bound forms are dynamically averaged over disordered conformational ensembles, the chemical shifts are relatively insensitive to differences in the conformational distribution resulting from metal binding. Therefore, we propose a model where, in the absence of pronounced conformational differences, metal binding to the disordered hZIP4 intracellular region influences the propensity for post-translational modifications through a change in the surface charge distribution. Our results provide evidence for long-range contacts between the metal-binding site and putative sites of post-translational protein modifications, which regulate plasma membrane levels of the hZIP4 protein, and provide a framework for future studies addressing the impact of post-translational modifications both on the isolated ICL2 region as well as in the context of the full-length transporter. The high-affinity zinc binding by hZIP4 ICL2 via a disordered ensemble contrasts with the disorder–order transition frequently involved in the biological functions of IDPs/IDRs.

Materials and Methods

Protein expression and purification

The ICL2 gene, corresponding to amino acid residues 424–498 in the full-length hZIP4, with a C-terminal Strep tag was codon optimized for expression in *E. coli* and was synthesized as a C-terminal fusion to the *E. coli pagP* gene lacking the signal sequence, a His_6 tag and a tobacco etch virus (TEV) protease cleavage sequence (GenScript, Piscataway, NJ). The resulting PagP-His_6-TEV-ICL2-Strep construct in pET3a was transformed into *E. coli* BL21(DE3) pLysS cells and grown in M9 minimal medium. ^{15}N- and $^{15}N/^{13}C$-labeled samples were prepared using 1 g L^{-1} $^{15}NH_4Cl$ and 3.5 g L^{-1} uniformly labeled ^{13}C-labeled glucose as sole nitrogen and carbon sources. Cells were grown to an optical density of 0.8, induced with 1 m*M* isopropyl-1-thio-β-D-galactopyranoside at 37°C for 5 hours, and harvested by centrifugation. Cells were resuspended in 20 m*M* Tris pH 8, 300 m*M* NaCl, 10% (v/v) glycerol, and 1 m*M* phenylmethylsulfonyl fluoride (PMSF) and lysed by sonication. Inclusion bodies were separated from the lysate by centrifugation at 100,000*g*, washed twice in 10 m*M* Tris pH 8, 50 m*M* NaCl, 0.5% (v/v) TritonX-100, 1 m*M* PMSF and washed once in 10 m*M* Tris pH 8, 50 m*M* NaCl, 1 m*M* PMSF. Inclusion bodies were solubilized in denaturing buffer (8 M urea, 100 m*M* Na_2HPO_4, 10 m*M* Tris pH 8) for 2 hours at room temperature. Following centrifugation for 30 min at 100,000*g*, solubilized inclusion bodies were loaded on cOmplete™ His-Tag Purification Resin (Millipore Sigma, St. Louis, MO) overnight at 4°C with agitation. After washing the column with denaturing buffer with 5 m*M* imidazole, protein was eluted in denaturing buffer with 200 m*M* imidazole. The eluted protein was supplemented with 0.4% (w/v) N-dodecyl-β-D-maltoside

and dialyzed against 10 m*M* Tris (pH 8) with stepwise reduction of urea (4*M*, 2*M,* and 0*M*) over 48 hours. Dithiothreitol (DTT; 1 m*M*) and EDTA (0.5 m*M*) were added to the dialyzed protein and cleavage of the fusion protein with TEV protease was carried out at room temperature for 2 hours. The cleaved protein was applied to a Strep-Tactin Superflow Resin (IBA Life Sciences, Göttingen, Germany). The column was washed with chelex-100 treated elution buffer (20 m*M* Hepes pH 7, 20% [v/v] glycerol). Protein was eluted in buffer containing 2.5 m*M* D-desthiobiotin. The binding affinity of the purified protein for zinc was measured using FluoZin-3 as described previously.[19] TCEP was added to a final concentration of 5 m*M*, and the protein was concentrated. Protein was quantified using the Reducing Agent Compatible Pierce™ Microplate BCA Protein Assay Kit (Thermo Fisher Scientific, Waltham, MA). Mutations were introduced into the codon-optimized PagP-His_6-TEV-ICL2-Strep construct using site-directed mutagenesis (Agilent Technologies, Santa Clara, CA) and were expressed and purified as described for the wild-type protein. Residues are numbered according to their position in the full-length hZIP4 amino acid sequence.

NMR spectroscopy

All NMR experiments were collected on an Agilent VNMRS 800 MHz spectrometer equipped with a cold probe. Resonance assignment experiments were performed using a 400 μ*M* sample of uniformly labeled $^{15}N/^{13}C$ protein in NMR buffer containing chelex-100-treated 20 m*M* Hepes pH 7, 20% (v/v) glycerol, 5 m*M* TCEP, 0.02% sodium azide, and 7.5% (v/v) ^2H_2O with EDTA-free protease inhibitors (Roche). NMR spectra were initially collected at 25°C with additional experiments conducted at 10°C. Backbone and side-chain resonances were assigned using two-dimensional ^1H-^{15}N HSQC and three-dimensional (3D) HNCO, HN(CA)CO, HNCACB, CBCA(CO)NH, HBHA(CO)NH, CCONH-TOCSY, and ^{15}N-edited NOESY-HSQC.[65] NMR data processing was done using software and computational resources in NMRbox (https://nmrbox.org/).[66] NMR spectra were processed using the Rowland NMR Toolkit (RNMRTK; http://rnmrtk.uchc.edu/rnmrtk/RNMRTK.html)[67] and analyzed using CcpNMR.[68] Secondary structure probabilities were estimated from the measured chemical shifts using the SSP score and the δ2D web server http://www-mvsoftware.ch.cam.ac.uk/index.php/d2D.[41,42] Chemical shift resonance assignments have been deposited in BioMagResBank with accession number 27321.

$^3J_{HN\text{-}H\alpha}$ coupling constants for ICL2 were obtained at 10°C using a 3D HNHA experiment with a phasing/dephasing delay of 13.41 ms.[69] Temperature coefficients were measured using ^1H-^{15}N HSQC spectra collected at 5° increments between 10°C and 25°C. Referencing was done using 2,2-dimethyl-2-silapentane sulfonate. Amide proton chemical shift values were plotted as a function of temperature, and temperature coefficients were calculated from the slope of the line ($\delta_H/\Delta T$) obtained by linear regression fitting.[70]

Backbone amide ^{15}N R_1, $R_{1\rho}$, and heteronuclear ^{15}N $\{^1H\}$ NOE relaxation measurements were performed at 10°C and 81 MHz ^{15}N Larmor frequency for 50 and 300 μ*M* samples of ^{15}N-labeled apoprotein and protein coordinated with one and two zinc ions.[71,72] R_1 values were acquired from a series of ^1H-^{15}N HSQC spectra with relaxation delays between 10 and 1000 ms. $R_{1\rho}$ relaxation rates were obtained using relaxation delay times between 10 and 120 ms. Spectra were processed using the relaxation data analysis features in NMRPipe.[73] R_1 and $R_{1\rho}$ values were calculated by fitting measured peak intensities to a single exponential decay. ^{15}N R_2 rates were obtained from R_1 and $R_{1\rho}$ rates measured at a spin-lock field strength of 1811.6 Hz.[74] ^{15}N $\{^1H\}$ NOE values were calculated from the ratios of peak intensities in ^1H-^{15}N correlation spectra acquired with and without proton saturation using a 5 s delay between spectra to ensure full recovery of ^{15}N longitudinal magnetization. Spectra were processed using RNMRTK,[67] and peak intensities were measured using CcpNMR.[67,68]

Backbone ^{15}N CPMG relaxation dispersion experiments with CPMG field strengths varying from 25 to 1000 Hz were recorded for 300 μ*M* protein samples at 10°C.[75] Spectra were processed using NMRPipe.[73] Relaxation dispersion profiles were generated using effective relaxation rates (R_{2eff}) calculated from intensities using

$$R_{2\text{eff}} = -\frac{1}{T_{\text{relax}}} \ln \frac{I}{I_0} \quad (1)$$

where T_{relax} is the constant relaxation delay and I_0 is the peak intensity measured in the absence of relaxation delay.

PRE experiments were performed using 50 μ*M* ^{15}N-labeled wild-type ICL2 that was spin labeled with MTSL (Toronto Research Chemicals, North York, ON, Canada) on the naturally occurring single cysteine (C436). MTSL-labeled protein was prepared as described.[76,77] For the labeling reaction, 300 μ*M* protein was treated with 2.5 m*M* DTT. The DTT was removed using a desalting column (Zeba spin desalting column; ThermoFisher Scientific, Waltham, MA), and the protein was immediately incubated with a 10-fold molar excess of MTSL for 15 minutes at room temperature. An additional 10-fold molar excess of MTSL was added, and the reaction was incubated overnight at room temperature. Unreacted MTSL was removed by buffer exchange (Amicon centrifugal filter, Millipore) into NMR buffer without TCEP. ^1H-^{15}N HSQC spectra were obtained at 10°C with 50 μ*M* MTSL-labeled protein and with the MTSL-labeled protein treated with a 5-fold molar excess of ascorbic acid for >3 hours to reduce the spin label. Spectra were processed using RNMRTK,[67] and peak

intensities for the paramagnetic (I_{ox}) and diamagnetic (I_{red}) states were measured using CcpNMR.[68] To calculate PRE distance restraints from the peak intensity ratios, the following equations were used[78]:

$$\frac{I_{ox}}{I_{red}} = \frac{R_2 e^{-R_2^{sp} t}}{R_2 + R_2^{sp}} \quad (2)$$

where R_2 is the amide proton transverse relaxation rate, R_2^{sp} is the relaxation contribution caused by the probe, and t is the evolution time of the proton during magnetization (10 ms)

$$r = \left[\frac{K}{R_2^{sp}} \left(4\tau_c + \frac{3\tau_c}{1 + \omega_h^2 \tau_c^2} \right) \right]^{\frac{1}{6}} \quad (3)$$

where r is the distance (in cm) between the amide proton and the paramagnetic probe, K is a constant (1.23×10^{-32} cm^6 s^{-2}) for the MTSL spin label, ω_h is the Larmor frequency of the ^{1}H, and τ_c is the apparent PRE correlation time. Ensembles of 10,000 statistical coil conformers were generated and theoretical PREs for the ensembles were computed using the *flexible-meccano* algorithm.[79] As a control for intermolecular effects of the spin label, ^{1}H-^{15}N HSQC spectra were obtained on a sample of 50 μ*M* MTSL-labeled ^{14}N-(wild-type)-ICL2 mixed with 50 μ*M* ^{15}N-C436A-ICL2 under nonreducing (paramagnetic) and reducing (diamagnetic) conditions.

Zinc binding

To prepare zinc-bound protein, $ZnCl_2$ (99.999% trace metals basis, Millipore Sigma, St. Louis, MO) stock solutions were prepared in chelex-100-treated elution buffer and quantified using a Zn^{2+}-terpyridine titration.[80] ^{1}H-^{15}N HSQC spectra were collected at 10°C on 300 μ*M* samples of ICL2 containing one and two molar equivalents of zinc. An additional spectrum was measured following addition of a five-fold molar excess of EDTA to the protein containing two equivalents of zinc. Spectra were processed using RNMRTK, and peak intensities and chemical shifts were measured using CcpNMR.[67,68] Chemical shift displacements (csd) were calculated according to the equation csd = $[(\Delta\delta H)^2 + (\Delta\delta N/5)^2]^{1/2}$.[81] ^{1}H-^{15}N HSQC spectra of the histidine side chains were acquired at 10°C with 602 complex points and an acquisition time of 108 ms. The insensitive nuclei enhanced by polarization transfer (INEPT) delay was 27.8 ms, and the carrier and spectral width values were 4.94 ppm and 9470 Hz in the direct dimension and 186.20 ppm and 12,800 Hz in the indirect dimension.[82]

Acknowledgments

We thank Dr. Alexandra Pozhidaeva for help with CCPNmr and Dr. Dmitry Korzhnev for help with the relaxation experiments and critical reading of the manuscript. We thank Spencer Pruitt for help setting up the *flexible-meccano* program. This work was supported by the National Institutes of Health (R01 GM105964) to R.E.D. This study made use of NMRbox: National Center for Biomolecular NMR Data Processing and Analysis, a Biomedical Technology Research Resource (BTRR), which is supported by National Institutes of Health grant P41GM111135 (NIGMS).

Conflict of Interest

The authors claim no conflict of interest.

References

1. Lipscomb WN, Strater N (1996) Recent advances in zinc enzymology. Chem Rev 96:2375–2434.
2. Andreini C, Banci L, Bertini I, Rosato A (2006) Counting the zinc-proteins encoded in the human genome. J Proteome Res 5:196–201.
3. Liang X, Dempski RE, Burdette SC (2016) Zn^{2+} at a cellular crossroads. Curr Opin Chem Biol 31:120–125.
4. Bafaro EM, Liu Y, Xu Y, Dempski RE (2017) The emerging role of zinc transporters in cellular homeostasis and cancer. Signal Trans Target Ther 2:17029.
5. Kambe T, Hashimoto A, Fujimoto S (2014) Current understanding of ZIP and ZnT zinc transporters in human health and diseases. Cell Mol Life Sci 71:3281–3295.
6. Küry S, Dréno B, Bézieau S, Giraudet S, Kharfi M, Kamoun R, Moisan J-P (2002) Identification of SLC39A4, a gene involved in acrodermatitis enteropathica. Nat Genet 31:239–240.
7. Wang K, Zhou B, Kuo Y-M, Zemansky J, Gitschier J (2002) A novel member of a zinc transporter family is defective in acrodermatitis enteropathica. Am J Hum Genet 71:66–73.
8. Schmitt S, Kury S, Giraud M, Dreno B, Kharfi M, Bezieau S (2009) An update on mutations of the SLC39A4 gene in acrodermatitis enteropathica. Hum Mutat 30:926–933.
9. Weaver BP, Zhang Y, Hiscox S, Guo GL, Apte U, Taylor KM, Sheline CT, Wang L, Andrews GK (2010) Zip4 (Slc39a4) expression is activated in hepatocellular carcinomas and functions to repress apoptosis, enhance cell cycle and increase migration. PLoS One 5:e13158.
10. Lin Y, Chen Y, Wang Y, Yang J, Zhu VF, Liu Y, Cui X, Chen L, Yan W, Jiang T, Hergenroeder GW, Fletcher SA, Levine JM, Kim DH, Tandon N, Zhu JJ, Li M (2013) ZIP4 is a novel molecular marker for glioma. Neuro Oncol 15:1008–1016.
11. Li M, Zhang Y, Liu A, Bharadwaj U, Wang H, Wang X, Zhang S, Liuzzi JP, Chang S-M, Cousins RJ (2007) Aberrant expression of zinc transporter ZIP4 (SLC39A4) significantly contributes to human pancreatic cancer pathogenesis and progression. Proc Natl Acad Sci USA 104:18636–18641.
12. Yang J, Zhang Y, Cui X, Yao W, Yu X, Cen P, Hodges SE, Fisher WE, Brunicardi FC, Chen C, Yao Q, Li M (2013) Gene profile identifies zinc transporters differentially expressed in normal human organs and human pancreatic cancer. Curr Mol Med 13:401–409.
13. Antala S, Ovchinnikov S, Kamisetty H, Baker D, Dempski RE (2015) Computation and functional studies provide a model for the structure of the zinc transporter hZIP4. J Biol Chem 290:17796–17805.
14. Zhang T, Liu J, Fellner M, Zhang C, Sui D, Hu J (2017) Crystal structures of a ZIP zinc transporter reveal a

binuclear metal center in the transport pathway. Sci Adv 3:e1700344.
15. Zhang T, Sui D, Hu J (2016) Structural insights of ZIP4 extracellular domain critical for optimal zinc transport. Nat Commun 7:11979.
16. Wang F, Kim B-E, Dufner-Beattie J, Petris MJ, Andrews G, Eide DJ (2004) Acrodermatitis enteropathica mutations affect transport activity, localization and zinc-responsive trafficking of the mouse ZIP4 zinc transporter. Hum Mol Genet 13:563–571.
17. Kambe T, Andrews GK (2009) Novel proteolytic processing of the ectodomain of the zinc transporter ZIP4 (SLC39A4) during zinc deficiency is inhibited by acrodermatitis enteropathica mutations. Mol Cell Biol 29: 129–139.
18. Mao X, Kim B-E, Wang F, Eide DJ, Petris MJ (2007) A histidine-rich cluster mediates the ubiquitination and degradation of the human zinc transporter, hZIP4, and protects against zinc cytotoxicity. J Biol Chem 282:6992–7000.
19. Bafaro EM, Antala S, Nguyen TV, Dzul SP, Doyon B, Stemmler TL, Dempski RE (2015) The large intracellular loop of hZIP4 is an intrinsically disordered zinc binding domain. Metallomics 7:1319–1330.
20. Peng Z, Yan J, Fan X, Mizianty MJ, Xue B, Wang K, Hu G, Uversky VN, Kurgan L (2015) Exceptionally abundant exceptions: comprehensive characterization of intrinsic disorder in all domains of life. Cell Mol Life Sci 72:137–151.
21. Minezaki Y, Homma K, Nishikawa K (2007) Intrinsically disordered regions of human plasma membrane proteins preferentially occur in the cytoplasmic segment. J Mol Biol 368:902–913.
22. Brown CJ, Johnson AK, Dunker AK, Daughdrill GW (2011) Evolution and disorder. Curr Opin Struct Biol 21: 441–446.
23. Wright PE, Dyson HJ (2015) Intrinsically disordered proteins in cellular signalling and regulation. Nat Rev Mol Cell Biol 16:18–29.
24. Tompa P, Fuxreiter M (2008) Fuzzy complexes: polymorphism and structural disorder in protein–protein interactions. Trends Biochem Sci 33:2–8.
25. Csizmok V, Follis AV, Kriwacki RW, Forman-Kay JD (2016) Dynamic protein interaction networks and new structural paradigms in signaling. Chem Rev 116:6424–6462.
26. Mollica L, Bessa LM, Hanoulle X, Jensen MR, Blackledge M, Schneider R (2016) Binding mechanisms of intrinsically disordered proteins: theory, simulation, and experiment. Front Mol Biosci 3:52.
27. Zhou H-X (2012) Intrinsic disorder: signaling via highly specific but short-lived association. Trends Biochem Sci 37:43–48.
28. Heller GT, Sormanni P, Vendruscolo M (2015) Targeting disordered proteins with small molecules using entropy. Trends Biochem Sci 40:491–496.
29. Borgia A, Borgia MB, Bugge K, Kissling VM, Heidarsson PO, Fernandes CB, Sottini A, Soranno A, Buholzer KJ, Nettels D (2018) Extreme disorder in an ultrahigh-affinity protein complex. Nature 555:61–66.
30. Shen Q, Shi J, Zeng D, Zhao B, Li P, Hwang W, Cho J-H (2018) Molecular mechanisms of tight binding through fuzzy interactions. Biophys J 114:1313–1320.
31. Jensen MR, Zweckstetter M, Huang J-R, Blackledge M (2014) Exploring free-energy landscapes of intrinsically disordered proteins at atomic resolution using NMR spectroscopy. Chem Rev 114:6632–6660.
32. Kosol S, Contreras-Martos S, Cedeño C, Tompa P (2013) Structural characterization of intrinsically disordered proteins by NMR spectroscopy. Molecules 18: 10802–10828.
33. Gibbs EB, Cook EC, Showalter SA (2017) Application of NMR to studies of intrinsically disordered proteins. Arch Biochem Biophys 628:57–70.
34. Hwang PM, Pan JS, Sykes BD (2012) A PagP fusion protein system for the expression of intrinsically disordered proteins in *Escherichia coli*. Protein Expr Purif 85: 148–151.
35. Hwang PM, Pan JS, Sykes BD (2014) Targeted expression, purification, and cleavage of fusion proteins from inclusion bodies in *Escherichia coli*. FEBS Lett 588:247–252.
36. Oldfield CJ, Dunker AK (2014) Intrinsically disordered proteins and intrinsically disordered protein regions. Annu Rev Biochem 83:553–584.
37. Wishart DS, Case DA (2001) Use of chemical shifts in macromolecular structure determination. Methods Enzymol 338:3–34.
38. Cavalli A, Salvatella X, Dobson CM, Vendruscolo M (2007) Protein structure determination from NMR chemical shifts. Proc Natl Acad Sci USA 104:9615–9620.
39. Kjaergaard M, Brander S, Poulsen FM (2011) Random coil chemical shift for intrinsically disordered proteins: effects of temperature and pH. J Biomol NMR 49: 139–149.
40. Tamiola K, Acar B, Mulder FA (2010) Sequence-specific random coil chemical shifts of intrinsically disordered proteins. J Am Chem Soc 132:18000–18003.
41. Marsh JA, Singh VK, Jia Z, Forman-Kay JD (2006) Sensitivity of secondary structure propensities to sequence differences between α-and γ-synuclein: implications for fibrillation. Protein Sci 15:2795–2804.
42. Camilloni C, De Simone A, Vranken WF, Vendruscolo M (2012) Determination of secondary structure populations in disordered states of proteins using nuclear magnetic resonance chemical shifts. Biochemistry 51:2224–2231.
43. Delaforge E, T. Cordeiro T, P. Bernadó P , and N. Sibille N Conformational characterization of intrinsically disordered proteins and its biological significance. In: Webb GA, Ed. (2017) Modern magnetic resonance. Cham, Switzerland: Springer International Publishing, pp 1–20.
44. Pelton J, Torchia DA, Meadow N, Roseman S (1993) Tautomeric states of the active site histidines of phosphorylated and unphosphorylated IIIGlc, a signal transducing protein from *Escherichia coli*, using two dimensional heteronuclear NMR techniques. Protein Sci 2:543–558.
45. Urbani A, Bazzo R, Nardi MC, Cicero DO, De Francesco R, Steinkühler C, Barbato G (1998) The metal binding site of the hepatitis C virus NS3 protease A spectroscopic investigation. J Biol Chem 273:18760–18769.
46. Chaudhury S, Nordhues BA, Kaur K, Zhang N, De Guzman RN (2015) NMR characterization of the type III secretion system tip chaperone protein PcrG of *Pseudomonas aeruginosa*. Biochemistry 54:6576–6585.
47. Korchuganov DS, Gagnidze IE, Tkach EN, Schulga AA, Kirpichnikov MP, Arseniev AS (2004) Determination of protein rotational correlation time from NMR relaxation data at various solvent viscosities. J Biomol NMR 30: 431–442.
48. Silvestre-Ryan J, Bertoncini CW, Fenwick TB, Esteban-Martin S, Salvatella X (2013) Average conformations determined from PRE data provide high-resolution maps of transient tertiary interactions in disordered proteins. Biophys J 104:1740–1751.
49. Kim B-E, Wang F, Dufner-Beattie J, Andrews GK, Eide DJ, Petris MJ (2004) Zn^{2+}-stimulated endocytosis of the mZIP4 zinc transporter regulates its location at the plasma membrane. J Biol Chem 279:4523–4530.
50. Kurochkina N, Guha U (2013) SH3 domains: modules of protein–protein interactions. Biophys Rev 5:29–39.

51. Austin Elam W, Schrank TP, Campagnolo AJ, Hilser VJ (2013) Evolutionary conservation of the polyproline II conformation surrounding intrinsically disordered phosphorylation sites. Protein Sci 22:405–417.
52. Remaut H, Waksman G (2006) Protein–protein interaction through β-strand addition. Trends Biochem Sci 31: 436–444.
53. Morgan JL, Jensen MR, Ozenne V, Blackledge M, Barbar E (2017) The LC8 recognition motif preferentially samples polyproline II structure in its free state. Biochemistry 56:4656–4666.
54. Taylor KM, Hiscox S, Nicholson RI, Hogstrand C, Kille P (2012) Protein kinase CK2 triggers cytosolic zinc signaling pathways by phosphorylation of zinc channel ZIP7. Sci Signal 5:ra11.
55. Valiente-Gabioud AA, Torres-Monserrat V, Molina-Rubino L, Binolfi A, Griesinger C, Fernández CO (2012) Structural basis behind the interaction of Zn^{2+} with the protein α-synuclein and the Aβ peptide: a comparative analysis. J Inorg Biochem 117:334–341.
56. Potocki S, Rowinska-Zyrek M, Valensin D, Krzywoszynska K, Witkowska D, Luczkowski M, Kozlowski H (2011) Metal binding ability of cysteine-rich peptide domain of ZIP13 Zn^{2+} ions transporter. Inorg Chem 50:6135–6145.
57. Potocki S, Valensin D, Camponeschi F, Kozlowski H (2013) The extracellular loop of IRT1 ZIP protein—the chosen one for zinc? J Inorg Biochem 127:246–252.
58. Kline CD, Gambill BF, Mayfield M, Lutsenko S, Blackburn NJ (2016) pH-regulated metal–ligand switching in the HM loop of ATP7A: a new paradigm for metal transfer chemistry. Metallomics 8:729–733.
59. Dyson HJ, Wright PE (2002) Coupling of folding and binding for unstructured proteins. Curr Opin Struct Biol 12:54–60.
60. Sugase K, Dyson HJ, Wright PE (2007) Mechanism of coupled folding and binding of an intrinsically disordered protein. Nature 447:1021–1025.
61. Arai M, Sugase K, Dyson HJ, Wright PE (2015) Conformational propensities of intrinsically disordered proteins influence the mechanism of binding and folding. Proc Natl Acad Sci USA 112:9614–9619.
62. Fuxreiter M (2018) Fuzziness in protein interactions–a historical perspective. J Mol Biol 430:2278–2287.
63. Miskei M, Antal C, Fuxreiter M (2016) FuzDB: database of fuzzy complexes, a tool to develop stochastic structure-function relationships for protein complexes and higher-order assemblies. Nucleic Acids Res 45:D228–D235.
64. Sharma R, Raduly Z, Miskei M, Fuxreiter M (2015) Fuzzy complexes: specific binding without complete folding. FEBS Lett 589:2533–2542.
65. Sattler M, Schleucher J, Griesinger C (1999) Heteronuclear multidimensional NMR experiments for the structure determination of proteins in solution. Progr Nucl Mag Res Sp 34:93–158.
66. Maciejewski MW, Schuyler AD, Gryk MR, Moraru II, Romero PR, Ulrich EL, Eghbalnia HR, Livny M, Delaglio F, Hoch JC (2017) NMRbox: a resource for biomolecular NMR computation. Biophys J 112:1529–1534.
67. Hoch JC, Stern AS. NMR data processing. New York: Wiley-Liss, 1996.
68. Vranken WF, Boucher W, Stevens TJ, Fogh RH, Pajon A, Llinas M, Ulrich EL, Markley JL, Ionides J, Laue ED (2005) The CCPN data model for NMR spectroscopy: development of a software pipeline. Proteins 59:687–696.
69. Kuboniwa H, Grzesiek S, Delaglio F, Bax A (1994) Measurement of H N-H α J couplings in calcium-free calmodulin using new 2D and 3D water-flip-back methods. J Biomol NMR 4:871–878.
70. Baxter NJ, Williamson MP (1997) Temperature dependence of ^{1}H chemical shifts in proteins. J Biomol NMR 9:359–369.
71. Farrow NA, Muhandiram R, Singer AU, Pascal SM, Kay CM, Gish G, Shoelson SE, Pawson T, Forman-Kay JD, Kay LE (1994) Backbone dynamics of a free and a phosphopeptide-complexed Src homology 2 domain studied by ^{15}N NMR relaxation. Biochemistry 33:5984–6003.
72. Korzhnev DM, Skrynnikov NR, Millet O, Torchia DA, Kay LE (2002) An NMR experiment for the accurate measurement of heteronuclear spin-lock relaxation rates. J Am Chem Soc 124:10743–10753.
73. Delaglio F, Grzesiek S, Vuister GW, Zhu G, Pfeifer J, Bax A (1995) NMRPipe: a multidimensional spectral processing system based on UNIX pipes. J Biomol NMR 6:277–293.
74. Massi F, Johnson E, Wang C, Rance M, Palmer AG (2004) NMR $R_{1\rho}$ rotating-frame relaxation with weak radio frequency fields. J Am Chem Soc 126:2247–2256.
75. Hansen DF, Vallurupalli P, Kay LE (2008) An improved ^{15}N relaxation dispersion experiment for the measurement of millisecond time-scale dynamics in proteins. J Phys Chem 112:5898–5904.
76. Sjodt M, Macdonald R, Spirig T, Chan AH, Dickson CF, Fabian M, Olson JS, Gell DA, Clubb RT (2016) The PRE-derived NMR model of the 38.8-kDa tri-domain IsdH protein from *Staphylococcus aureus* suggests that it adaptively recognizes human hemoglobin. J Mol Biol 428:1107–1129.
77. Sjodt M, Clubb RT (2017) Nitroxide labeling of proteins and the determination of paramagnetic relaxation derived distance restraints for NMR studies. Bio-Protocol 7:e2207.
78. Battiste JL, Wagner G (2000) Utilization of site-directed spin labeling and high-resolution heteronuclear nuclear magnetic resonance for global fold determination of large proteins with limited nuclear overhauser effect data. Biochemistry 39:5355–5365.
79. Ozenne V, Bauer F, Salmon L, Huang J-R, Jensen MR, Segard S, Bernadó P, Charavay C, Blackledge M (2012) Flexible-meccano: a tool for the generation of explicit ensemble descriptions of intrinsically disordered proteins and their associated experimental observables. Bioinformatics 28:1463–1470.
80. Burdette SC, Walkup GK, Spingler B, Tsien RY, Lippard SJ (2001) Fluorescent sensors for Zn^{2+} based on a fluorescein platform: synthesis, properties and intracellular distribution. J Am Chem Soc 123:7831–7841.
81. Doyle CM, Rumfeldt JA, Broom HR, Sekhar A, Kay LE, Meiering EM (2016) Concurrent increases and decreases in local stability and conformational heterogeneity in Cu,Zn superoxide dismutase variants revealed by temperature-dependence of amide chemical shifts. Biochemistry 55:1346–1361.
82. Rezaei-Ghaleh N, Andreetto E, Yan L-M, Kapurniotu A, Zweckstetter M (2011) Interaction between amyloid beta peptide and an aggregation blocker peptide mimicking islet amyloid polypeptide. PLoS One 6:e20289.